

Origami-based Invaginatable Soft Vacuum Actuators with Optimized Creases that Avoid Bending Stress Concentration

Keisuke Kayama,* Noriyasu Iwamoto, and Takuya Umedachi

Faculty of Textile Science and Technology, Shinshu University, 3-15-1 Tokida, Ueda, Nagano 386-8567, Japan

(Received February 27, 2023; accepted May 16, 2023)

Keywords: soft actuator, folding structure, soft material, biomimetics

We developed actuators that can be invaginated, combining a vacuum-pressure drive with a folding structure with durable creases, which were optimized by our proposed method. In this paper, we propose two types of prototype actuator: linear and bending. The advantage of invagination actuators is that the amount of deformation (i.e., linear deformation in the linear model and deformation angle of the tip in the bending model) can be increased and be determined at the design stage. The deformation results for this actuator showed that the total length becomes more than 50% smaller for the resting length of a three-modulus linear model, and the tip rotated 179.3° for the three-modulus bending model. The error between the design and the resulting deformation was less than 1%. In addition, the problem of bending stress concentration and rupture at the actuator's creases during folding deformation is alleviated by redesigning the shape of the creases through our proposed approach of optimizing the cross-sectional crease shape. As a result, the fabricated actuator has shown a durability of more than 100000 actuation cycles. This actuator design will increase the applications of grippers and soft robots and improve the lifetime of the soft actuator.

1. Introduction

Living organisms can not only extend and contract but also invaginate their body surface, which leads to movements with large volume changes. An example of such deformation is a male beetle larva that grows horns when it becomes a pupa.⁽¹⁾ The horns that have been folded and kept wrinkled grow large when it is pressurized by body fluids. Arthropods also utilize such invagination between segments to have joints (creases) even though they have hard shells. In particular, a pill bug can transform between two forms: linear and spherical.

Such arthropod growth and morphology-changing deformation are accomplished by folding the body surface(s). There are a few examples of such origami structures in soft pneumatic actuators (SPAs).⁽²⁾ This folding mechanism can avoid rupture owing to the excessive stretching of flexible material compared with inflatable pneumatic actuators. In addition, the creases limit the degree of freedom of deformation, making it easy to design the shapes before and after deformation. An example of origami structures in a soft pneumatic actuator is the 3D printed

*Corresponding author: e-mail: kayamaforuniv@gmail.com
<https://doi.org/10.18494/SAM4365>

linear soft vacuum actuator (LSOVA),⁽²⁾ which is driven by a vacuum pressure source and has improved durability due to folding of the membrane wall. However, actuators with creases have the problem that the creases break due to bending stress concentration. The bending stress concentration is also an issue in research where a 3D printer is used to create a structure that folds and changes in volume.⁽³⁾

In this study, we developed an invaginatable and foldable soft pneumatic actuator with cross-sectional crease shapes that avoid bending stress concentration, driven by a vacuum pressure source. As shown in Figs. 1(a) and 1(c), the advantage of employing folding in pneumatic actuators is that the volume can be reduced by bending and deforming the continuous sheet or membrane while maintaining its sealability (avoiding air leakage). This allows for a more extensive range of motion for the actuator. The actuator is designed to deform drastically during invagination. In addition to this folding mechanism, a fail-safe mechanism provided by the vacuum drive aims for durability and deformation as designed. Furthermore, the creases, which are a bottleneck in the durability of folding actuators, are created from optimized cross-sectional crease shapes. We use optimization to find the cross-sectional crease shape that minimizes the maximum bending stress calculated by physical simulation. A soft robot driven by such soft actuators would be suitable for cooperative work with humans.

In this paper, we propose two types of prototype actuators: linear and bending. We optimize the crease shape for each model and evaluate their deformation and durability. First, in Sect. 2, we describe the related works. Second, in Sect. 3.1, we present a design procedure for the invaginatable actuators, including the effect of the membrane thickness on the design. Next, in Sect. 3.2, we present an optimization method for the crease shapes to avoid bending stress concentration. Then, in Sect. 4, we evaluate the results of the optimal cross-sectional crease shapes and the durability and deformation of the actuator. Finally, we discuss an additional advantage of the optimized model and give conclusions and future perspectives.

2. Related Works

Vacuum-driven soft pneumatic actuators have recently been developed,^(4–7) in contrast to soft pneumatic actuators driven by positive pressure.^(8–12) One advantage of such actuators is that we

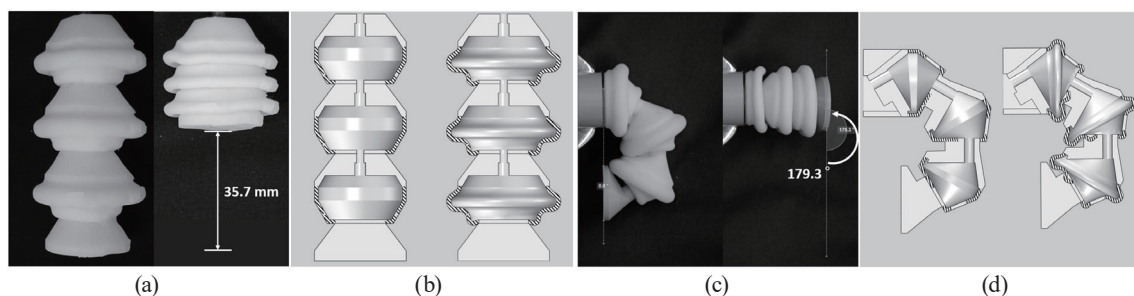


Fig. 1. Deformations of (a) a linear deforming actuator and (c) a bending actuator. (b) and (d) show the cross-sectional crease shapes of each actuator, with the right actuator having an optimized shape at the crease where bending stress is not concentrated compared with the left actuator.

can avoid excessive deformation and rupture with too much pressure, allowing for a fail-safe feature against excessive air pressure caused by machine malfunction. Thus, the final positioning accuracy and durability after deformation are improved. Another advantage is applicability in narrow spaces, as the structure deforms while contracting.⁽²⁾

A number of studies utilizing origami for robotics and shape design have attracted considerable attention.⁽¹³⁾ Origami-based structures with semisoft folds and creases are compliant to absorbing external shocks through deformation. Folding structures that utilize material deformation have the ability to recover to their original shape.

In this paper, we propose a 3D-printable actuator that combines a soft origami membrane structure and a vacuum drive. Similar actuators have been proposed in terms of the combination of pneumatic or vacuum pressure with origami.^(14–16) However, the weakness of those actuators is durability: they could not be used for a long time because of stress concentration in the creases. Using 3D printing technology, which allows us to create the complex structures with less effort, we incorporate optimized creases to reduce the maximum bending stress into the actuators, which will be described below.

3. Proposed Method

3.1 Design of actuators

3.1.1 Design concept: Invagination folding of flexible materials

We show how to design the proposed actuator that utilizes the invagination of deformable materials. We need to pay attention to membrane thickness as a precaution in designing this actuator. In other words, the folding membrane should be thin, but it must be sufficiently thick to withstand the vacuum pressure and to be printed by a 3D printer.

To begin with, let us consider the design of a cone-shaped invaginatable actuator that has a thin membrane with ignorable thickness. In Fig. 2(a), a symmetry plane is placed to cut through the cone. In this paper, we define a convex fold as the valley and a concave fold as the mountain when we look at the actuator from the outside. We reduce the actuator's volume by folding the membrane with the crease curve at the intersection of the conical surface and the symmetry plane as a mountain crease and the apex of the cone as a valley crease. The conical portion above the symmetry plane and another conical portion mapped in a mirror image to the plane [depicted with gray dotted lines in Fig. 2(a)] show the deformed part before and after deformation, respectively. The air chamber will be the volume (bounded by the conical portions) where the membrane moves. Since the membrane thickness is not considered, the air chamber is symmetrical with the plane of symmetry. The part excluding the membrane and the air chamber is the thick membrane in the figure.

Next, Fig. 2(b) shows the actuator design considering the membrane thickness. Here, the air chamber and the membrane thickness are designed. For simplicity of design in this study, the membrane wall is built inward along the outline of the conical portion above the symmetry plane and is called the thin membrane [Fig. 2(b), arrows above the symmetry plane]. The thickness of

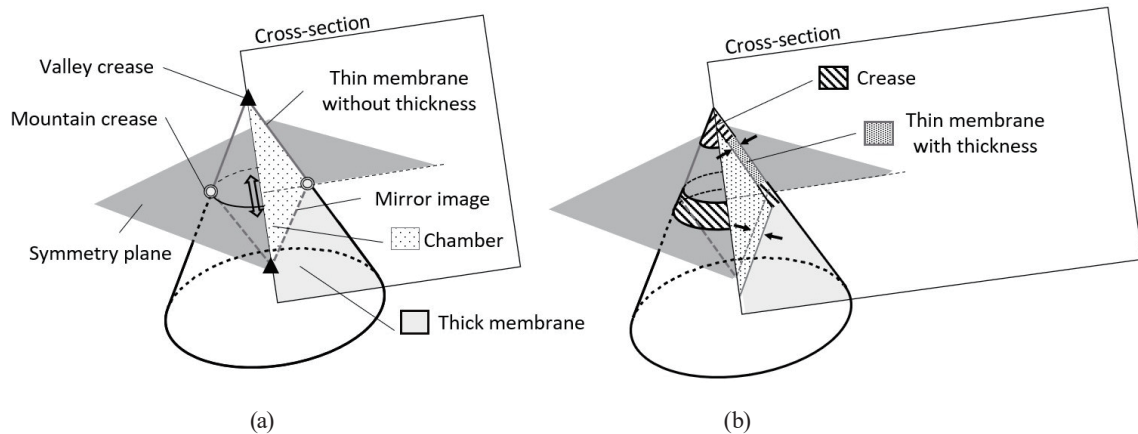


Fig. 2. Design methods and transformations for folding actuators (a) without and (b) with thin membrane thickness.

the thin membrane should be smaller than that of the thick membrane to facilitate deformation. Adding the thin membrane increases the volume of the deformed shape by the thickness of the thin membrane. Therefore, we increase the volume of the air chamber by shaving off the thick membrane to create a space where the deformed thin membrane can be placed [Fig. 2(b), arrows below the symmetry plane].

3.1.2 Folding of crease having thickness

The crease of the proposed pneumatic actuator requires the setting of the rotation axis among O_{IN} , $O_{MEMBRANE}$, and O_{OUT} in Fig. 3(a) and the crease width [depicted as stripe pattern in Fig. 3(a)]. In material mechanics, the axis of rotation is generally $O_{MEMBRANE}$. However, the above method of adding membrane thickness from the outer shape [Fig. 2(b)] requires that O_{OUT} be the axis of bending deformation. In Sect. 3.2, we will describe the design of the shape of the crease.

Here, we describe how to set the crease width. Bending at the crease is caused by the material's deformation near the rotation axis. Therefore, we set the crease width to be larger than the deformation, as shown in Fig. 3(a). The thicker the membrane, the wider the deformation is expected to be. In detail, in Figs. 3(b) and 3(c), the mountain folding is a bending deformation with contraction of the membrane, and the valley folding is a bending deformation with extension. The crease width must be at least wider than the overlapping area [dark gray stripe pattern in Fig. 3(b)] for the valley crease. The larger the bending crease angle and membrane thickness, the wider the crease width should be.

3.1.3 Prototype design

In this study, we propose two types of actuator: a linear model that deforms in a straight line and a bending model that deforms in a bend, as shown in Fig. 1. Figures 4(a) and 4(b) show the method of designing each outer shape from a cone. We cut the cone with the symmetry plane parallel to the base [Figs. 4(a) and 4(b) black plane], and we further cut the small cone with a

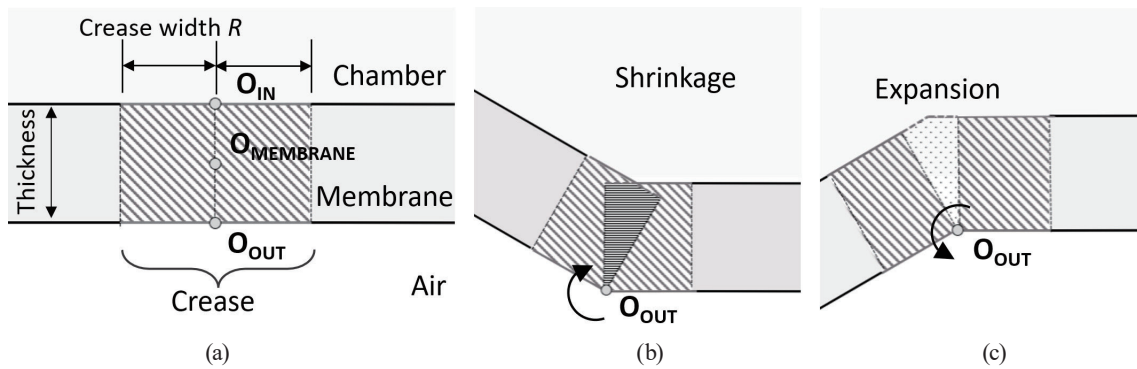


Fig. 3. Bending a thick crease at axis O_{OUT} . The mountain folding causes shrinkage (overlap) on the air chamber side, and the valley folding leads to expansion on the air chamber side.

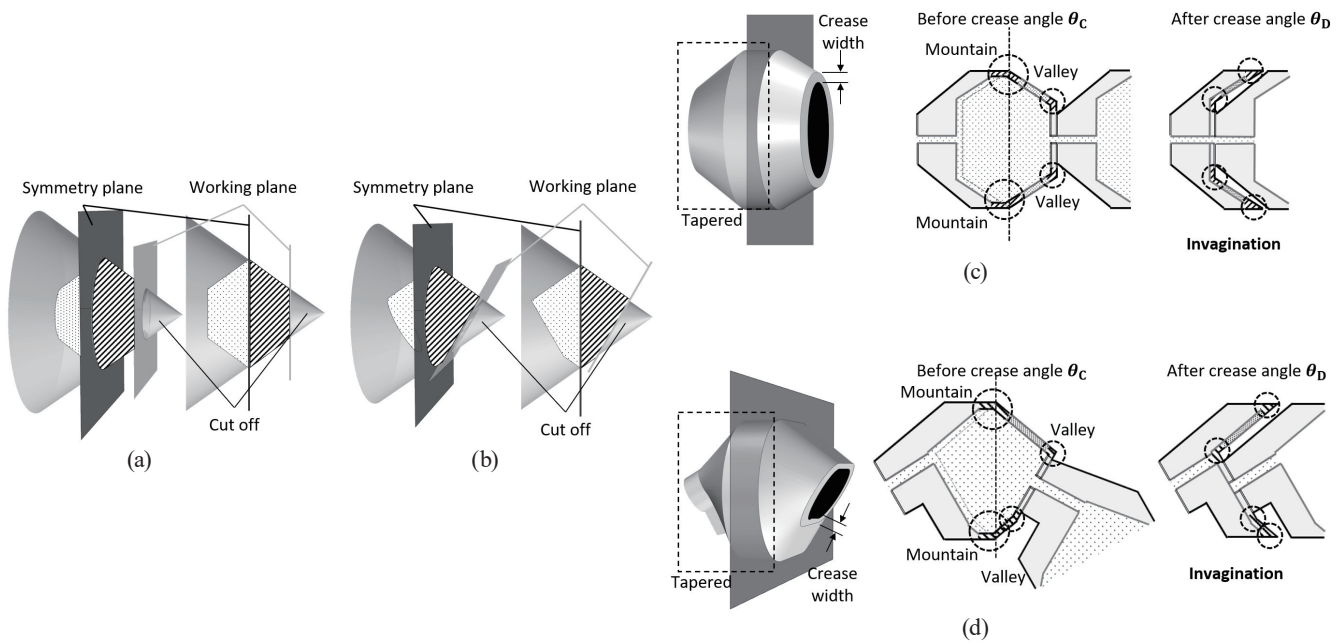


Fig. 4. Design of linear and bending models. (a) and (b) are the methods to create the straight-line model and a bending model from a cone. (c) and (d) are modular shapes with tapered thick membranes and show illustrations of the cross-sectional view of the actuators combined with the module and their transformations.

working plane [Figs. 4(a) and 4(b) gray plane]. In a linear model, the working plane is placed parallel to the symmetry plane. In the bending model, the working plane is placed at an angle. Stripe and dot patterns in Figs. 4(a) and 4(b) are the deformed portions and their mirror images, respectively. The edge of the area where the symmetry plane and the cone intersect is the crease curve as the mountain crease, and the edge of the area where the working plane and the cone intersect is the crease curve as the valley crease. The sections cut by these working planes, which are moved by air extraction and insertion, move linearly in Fig. 4(a) and tilt in Fig. 4(b). Thus, in the linear model, the distance between the symmetry plane and the working plane is the

displacement. In the bending model, the angle between the symmetry plane and the working plane is the bending angle.

The design process for connecting actuators in series to form a single actuator is explained. The thick membrane part should be cut away along the shape of the air chamber, maintaining the thickness of the thick membrane, which forms a conical shape. As shown in Figs. 4(c) and 4(d), the shape of the conical base [left part of the symmetry plane in Figs. 4(c) and 4(d)] is tapered and modularized. The tapered tips should be the size of the cut surface minus the crease width. We apply the same membrane thickness treatment to these actuators that we described in Sect. 3.1.1 for the cone actuator. The angles before and after the deformation of these creases can be determined from the relative position between the cone shapes, the position of the symmetry plane, and the working plane.

3.2 Optimization of crease shape

We design the cross-sectional crease shape to avoid bending stress concentration, which leads to the 3D crease design. This is because it is difficult to optimize the entire 3D crease shape at once. This method of crease shape design requires that the crease curve is a simple closed curve (i.e., Jordan curve). The cross-sectional crease shapes before optimization are the cross-sectional shapes with the crease divided perpendicular to the crease curve. We optimize each cross-sectional crease shape by the method (Fig. 5) described below. All optimized cross-sectional crease shapes will be loosely connected along the closed curves to create a 3D crease shape. In this subsection, we describe a design method for the cross-sectional crease shape, including the optimization and software used.

3.2.1 Cross-sectional crease shape parameters used for optimization

For the optimization, we design multiple cross-sectional crease shapes using parameters that represent an interpolation curve and a different thickness distribution [Fig. 6(b)] based on the cross-sectional crease shape before optimization [Fig. 6(a)]. The process will be described below.

First, we determine the crease width R at the cross-sectional crease shape [Fig. 6(a)]. Bending stress concentration is avoided by distributing the crease deformation areas. We set lines AP and PB to be the neutral lines (planes) of the crease before optimization [Fig. 6(a)], and their lengths will be the same. With the angle bisector of lines AP and PB as the symmetry axis, this cross-sectional shape has a symmetrical form.

Secondly, we set P' on the symmetry axis, which is a representative point to draw the interpolation curve. Here, P' moves on the angle bisector. The position of P' is determined by the vector \vec{u} (toward point P' from point P). Using a variable a and a unit vector \vec{e} toward the air chamber on the angle bisector, we represent \vec{u} as

$$\vec{u} = a\vec{e}. \quad (1)$$

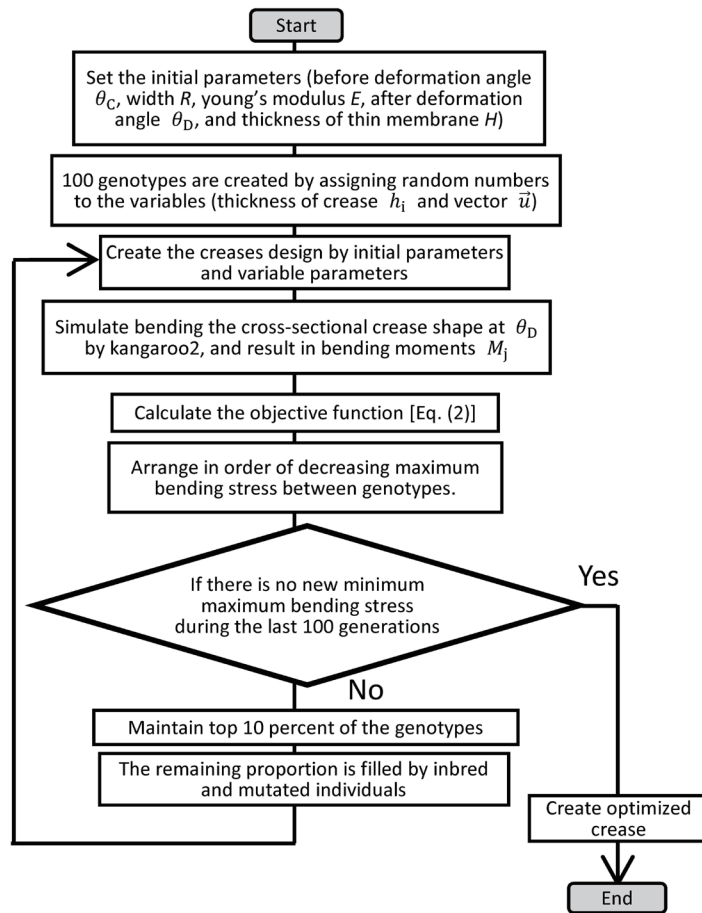


Fig. 5. Flowchart for optimizing cross-sectional crease shape to minimize maximum bending stress.

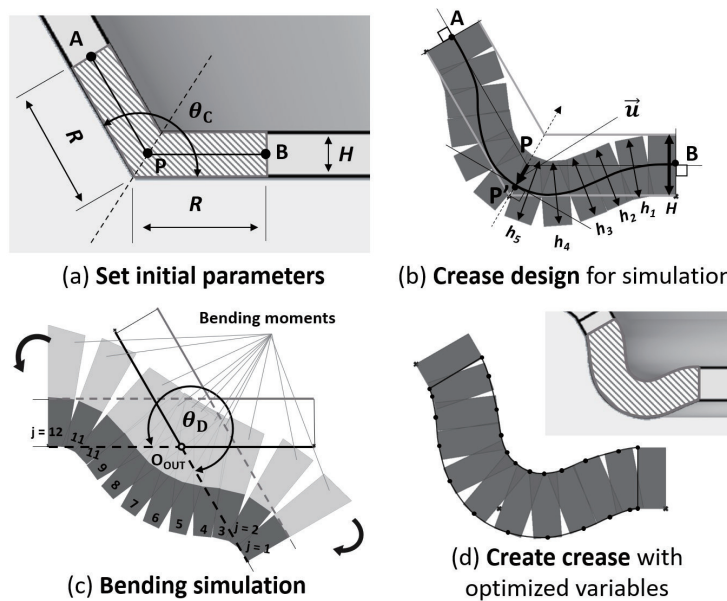


Fig. 6. Design method by optimizing the cross-sectional crease shape.

Then, the interpolation curve (that determines the approximate cross-sectional crease shape) is created by connecting the three points, A, P', and B, where the tangents of this curve at endpoints A and B should coincide with the straight lines AP and PB, respectively.

In addition to this, the cross-sectional crease shape is designed with the crease membrane thickness distribution h_i ($1 \leq i \leq 5$) as the other parameter. The symmetry allows the thickness of the 12 segments (including endpoint segments whose thickness is H) to be designed using five parameters, h_i .

3.2.2 Optimization method and evaluation function

We simulate the bending of the cross-sectional crease shape into the designed angle and seek the optimal design parameters to minimize the maximum bending stress. The designed angle refers to a target angle after the bending deformation of the cross-sectional crease shape. In this study, we optimize the cross-sectional crease shapes individually (obtained from dividing the crease curve). After the optimization, which will be explained in the following, we will connect the optimized cross-sectional crease shapes, to reduce the overall bending stress.

The cross-sectional crease shape is discretized into 12 sections, and bending deformation is simulated using the Kangaroo2 component "Beam". The section thickness is h_j ($1 \leq j \leq 12$). h_j is constituted from h_i and H by symmetry, as shown in Fig. 6(b). The parameters required for the simulation are the crease width R , the before crease angle θ_C , the designed angle θ_D (i.e., after crease angle), Young's modulus E of the material used, \bar{u} that determines the approximate cross-sectional crease shape, and the area moment of inertia I_j obtained from h_j .

The bending simulation results in the bending moments M_j for the 12 sections. The bending stress σ_j occurring at the crease can be expressed as

$$\sigma_j = \frac{M_j \left(\{h_j\}_{j=1}^{12}, a \right) h_j}{I_j(h)_j} \cdot \frac{1}{2}. \quad (2)$$

$$\begin{aligned} &\text{minimize} && \max(\sigma_j), \\ &\text{subject to} && h_i, a \in \Omega. \end{aligned}$$

The range of random numbers Ω depends on the linear model or bending model (which will be explained in Sect. 4). The lower limit of h_i is determined by the accuracy of the 3D printer used. The upper limit of h_i must be a thickness value such that the crease does not self-intersect during the bending simulation. If the range of a is too large, the protrusion or concavity of the actuator crease will be too large, and interference with other parts of the actuator can occur. Therefore, the range of a must be small enough to prevent such interference. We minimize the maximum bending stress $\max(\sigma_j)$ in each cross-sectional crease shape.

3.2.3 Optimization software

We use Grasshopper, a modeling aid plug-in for Rhinoceros that can simulate, optimize, and design crease cross sections simultaneously. Kangaroo2, a physics simulation plug-in for Grasshopper, can simulate bending using the dynamic relaxation (DR) method.⁽¹⁷⁾ DR is a straightforward iterative method of finding a static equilibrium state by artificially converting a static system into a dynamic one and minimizing the total potential energy in the structure by applying virtual inertia and damping forces. First, the static positions of the 12 segments are searched for by dividing and discretizing the cross-sectional crease shape and integrating them over time for a definitive solution. Galapagos (a component of Grasshopper) and the genetic algorithm (an evolutionary solver) are used as the optimization methods.

4. Result

4.1 Fabrication of the actuator

The dimensions of one module of the designed linear and bending models are shown in Fig. 7. The base of the cone [Figs. 4(a) and 4(b)] is circular in the linear model and oval in the bending model. This oval is a combination of a circle and a rectangle. We set the crease width R to be 4.13 mm (mountain crease) and 2.29 mm (valley crease) for the linear model, and 4.00 mm (mountain crease) and 2.50 mm (valley crease) for the bending model. We printed three modules connected together using a 3D printer [Figs. 1(a) and 1(c)]. The sizes and masses of these fabricated actuators are shown in Table 1. The 3D printer is MITs M3DS-SA5, and the material is Shore A5 reinforced rubber-like resin.

4.2 Results of crease optimization

We optimized the cross-sectional crease shape from Figs. 7(a) and 7(c) to Figs. 8(a) and 8(b). In the linear model, cross-sectional crease shapes on the single crease curve (mountain crease or valley crease) have the same shape. In detail, the before crease angle θ_C and the designed angle θ_D in each cross-sectional crease shape is the same. Therefore, we optimized only ① and ② in

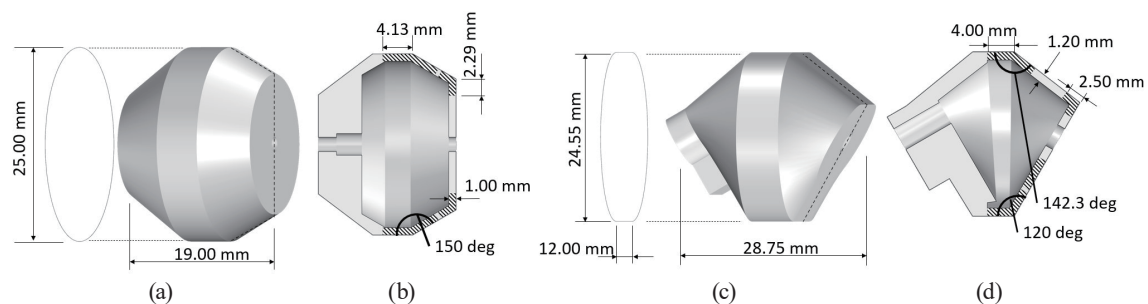


Fig. 7. Dimensions of (a, b) the linear model and (c, d) bending model.

Table 1
Parameters and performance of actuators.

Linear actuator		
m_L	Mass of linear actuator	17.79 g
L_{design}	Total length at design	67.0 mm
δ_{design}	Linear deformation at design	36.0 mm
δ_{result}	Actual linear deformation	35.7 mm
T	Lifetime	>100000
P	Pressure required for deformation	-5 kPa
Bending actuator		
m_B	Mass of bending actuator	31.08 g
R_{radius}	Radius of the sphere covering the actuator	3.5 mm
$\Delta\theta_{design}$	Deformation angle of tip at design	180°
$\Delta\theta_{result}$	Actual tip deformation angle	179.3°
t	Lifetime	>100000
P	Pressure required for deformation	-5 kPa

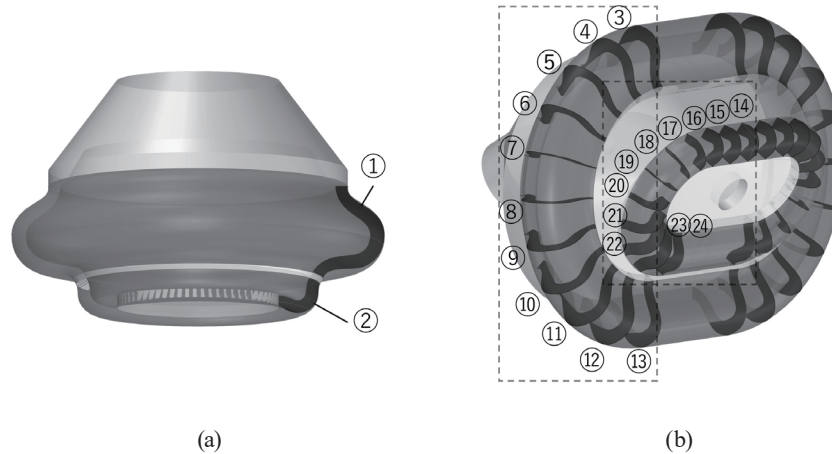


Fig. 8. Optimized cross-sectional crease shapes of the (a) linear model and (b) bending model. In the linear model, ① is a mountain crease and ② is a valley crease. ③–⑬ are mountain creases and ⑭–⑳ are valley creases.

Fig. 8(a), and swept along the crease curve. In the bending model, we optimized the 22 cross-sectional crease shapes, ③–㉔, in Fig. 8(b) and created the lofted surface by fitting the optimized cross-sectional crease shapes along the crease curves. We created the creases by solidifying this lofted surface.

The required initial parameters for optimization, in addition to the crease width and thin membrane thickness, are Young's modulus $E = 2.8$ MPa for Shore A5 reinforced rubber-like resin, the before crease angle θ_C (Table 2), and the designed angle θ_D . The designed angle θ_D of the two models is $180^\circ - \theta_C$ for the mountain creases and $360^\circ - \theta_C$ for the valley creases. Next, the range of random numbers Ω for the variable parameters h_i and a is $0.8 \cdot H \leq h \leq 1.2 \cdot H$, $-3 \leq a \leq 3$. The variable parameter a stands for \vec{u} (positive toward the air chamber in Fig. 6). In the genetic algorithm, we optimized cross-sectional crease shapes with the following conditions: 100 individuals, crossover of 70%, inheritance in the top 10%, and mutation of 20%.

Table 2
Optimized parameters.

	Linear		Bending																							
	①	②	③	④	⑤	⑥	⑦	⑧	⑨	⑩	⑪	⑫	⑬	⑭	⑮	⑯	⑰	⑱	⑲	⑳	㉑	㉒	㉓	㉔		
Optimized shape																										
θ_c	150°	120°	142.3°	141.1°	140.0°	138.7°	136.8°	134.2°	130.7°	126.7°	123.0°	120.5°	119.9°	97.7°	97.7°	97.7°	97.7°	101.1°	108.8°	120.5°	135.5°	151.7°	166.5°	176.7°	180.0°	
α (mm)	-3.00	-0.36	-3.0	-3.0	-3.0	-3.0	-3.0	-3.0	-3.0	-3.0	-3.0	-3.0	-3.0	-0.3	-0.3	-0.3	-0.3	-0.3	-0.4	-0.5	-0.6	-0.9	-1.0	-1.2	-1.2	
h_1 (mm)	1.03	0.99	1.15	1.13	1.12	1.08	1.03	1.04	1.02	1.10	1.06	1.17	1.17	1.20	1.20	1.20	1.20	1.18	1.19	1.18	1.17	1.20	1.27	1.23	1.23	
h_2 (mm)	0.98	1.01	1.17	1.17	1.17	1.16	1.17	1.17	1.02	1.18	1.18	1.20	1.20	1.21	1.21	1.21	1.21	1.18	1.20	1.20	1.21	1.23	1.27	1.27	1.27	
h_3 (mm)	1.07	1.03	1.28	1.28	1.28	1.28	1.28	1.28	1.28	1.29	1.29	1.30	1.30	1.27	1.27	1.27	1.27	1.22	1.23	1.24	1.28	1.26	1.34	1.33	1.33	
h_4 (mm)	1.15	1.06	1.38	1.38	1.38	1.38	1.38	1.38	1.38	1.39	1.39	1.39	1.39	1.25	1.25	1.25	1.25	1.25	1.24	1.27	1.36	1.30	1.41	1.38	1.38	
h_5 (mm)	1.20	1.08	1.44	1.44	1.44	1.44	1.44	1.44	1.44	1.44	1.44	1.44	1.44	1.26	1.26	1.26	1.26	1.26	1.25	1.29	1.40	1.35	1.44	1.41	1.41	
Maximum bending stress of fillet (N/mm ²)	-0.99	0.58	-0.64	-0.63	-0.62	-0.61	-0.59	-0.57	-0.54	-0.50	-0.46	-0.44	-0.43	0.58	0.58	0.58	0.58	0.55	0.49	0.39	0.28	0.16	0.07	0.01	0.00	
Maximum bending stress of optimization (N/mm ²)	-0.30	0.25	-0.17	-0.17	-0.16	-0.16	-0.15	-0.14	-0.13	-0.12	-0.10	-0.10	-0.09	0.24	0.24	0.24	0.24	0.24	0.21	0.17	0.12	0.08	0.03	0.01	0.00	
Decrement (%)	29.8	43.6	26.7	26.5	26.2	25.9	25.5	24.9	24.1	23.2	22.3	21.6	21.5	42.3	42.3	42.3	42.3	43.0	43.5	43.8	43.6	49.2	52.2	70.3	/	

Figures 9(a) and 9(b) show the bending stress distributions generated by the bending simulation of the filleted crease without the optimization and the optimized cross-sectional crease shapes in the linear model. The bending stress distribution of the mountain crease in the filleted linear model [Fig. 9(a)] shows stress concentrations at the edges and center of the cross-sectional crease shape. In the same figure, the distribution of the optimized linear model avoids the bending stress concentration, and the maximum stress at the crease is considerably reduced. The bending stress distribution of the valley crease in the filleted linear model [Fig. 9(b)] also shows stress concentrations at the edges of the crease. The distribution of the optimized linear model flattened the stresses in the creases and reduced the maximum stresses.

In the optimization result of the mountain crease, the bending stresses at the edge [1–2, 11–12 in Fig. 9(a)] and the center of the crease segments [3–10 in Fig. 9(a)] are different because the optimized variable a (which defines the cross-sectional crease shape, convex when negative and concave when positive) for the mountain crease is -3.0 , which is the range limit of Ω , according to the results in Table 2. We think that the optimal value of a would be even smaller (i.e., $a < -3$); however, if the value of a is too small, the membrane thickness and the shape of the interpolated curve will cause self-intersection.

Figures 10(a) and 10(b) show the bending stress distributions generated by the bending simulation of the filleted and optimized cross-sectional crease shapes in the bending model. The results are similar to the linear model results for the mountain crease and valley crease in the sense that stress concentrations are avoided.

The values in the second row from the bottom in Table 2 show that the maximum bending stresses of the optimized cross-sectional crease shapes became less than 1/3 in the mountain crease and 1/2 in the valley crease compared with those of the filleted cross-sectional crease shapes (the values in the third row from the bottom) in both linear and bending models. The tensile strength of the resin used in this study is 1.3 N/mm^2 , so the safety ratio is over 4. In reality, external forces such as air pressure and gravitation force will cause differences from the simulation results, which may cause more stress on the creases.

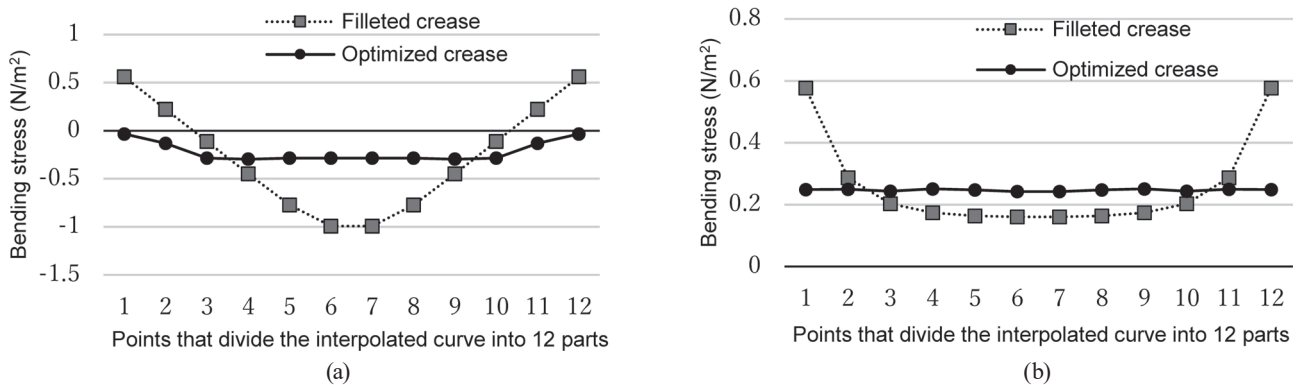


Fig. 9. Distribution of stresses acting on bending simulation of the cross-sectional crease shapes which are filleted and optimized in the linear model [(a) the mountain crease and (b) the valley crease.]

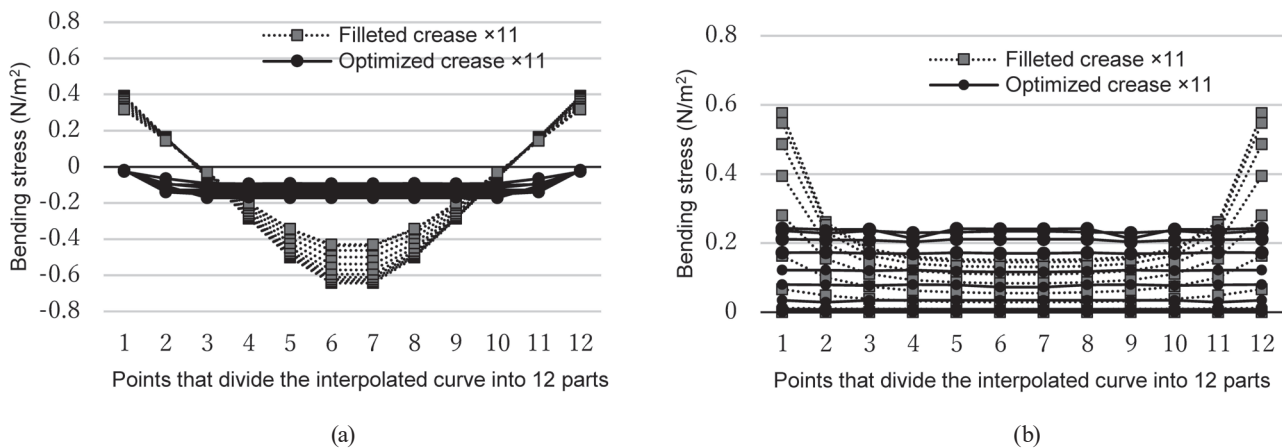


Fig. 10. Distributions of stresses acting on bending simulation of the cross-sectional crease shapes that are filleted and optimized in the bending model [(a) the mountain crease and (b) the valley crease].

4.3 Amount of deformation

For the linear model, the total lengths of the three-module actuator before and after deformation were measured when it was suspended with the air inlet at the top [Fig. 1(a)]. The total length of the actuator at the atmospheric pressure was 67.0 mm in modeling and 77.2 mm when suspended. This is because gravitational force stretches this soft actuator owing to its weight. The total length of the actuator after deformation at -10 kPa (gauge pressure), both suspended and lying on the floor, was 31.3 mm. The length changes were 53.2% smaller. The deformation error is less than 1% compared with the designed total length of 31.0 mm after deformation.

In the bending model, the rotational deformation of the tip module was measured for the three-module actuator lying on the floor in order to eliminate the deformation caused by gravitational force [Fig. 1(b)]. As can be seen in the figure, at -10 kPa (gauge pressure), the tip module rotated 179.3° , and the actuator shape transformed from a curled state to an approximately straight state. In the suspended state [gravity is applied in the downward direction in Fig. 1(c)], the actuator shape after deformation was the same as in the lying state. The rotational deformation error was less than 1% (the designed rotational deformation angle is 180°).

These deformation errors in the two models may be caused by the accuracy limitation of the 3D printing and the deformation of the thick membrane.

4.4 Lifetime and durability

The numbers of cycles until rupture of the two models, i.e., the three-module actuators, were measured when suspended in atmospheric pressure. These two models deform at -10 kPa (gauge pressure) and return to their original shape at atmospheric pressure due to the release of elastic energy stored in the creases. The reason for the suspended state is that it is difficult for these actuators to return to their original shapes, given that they are subjected to friction caused by

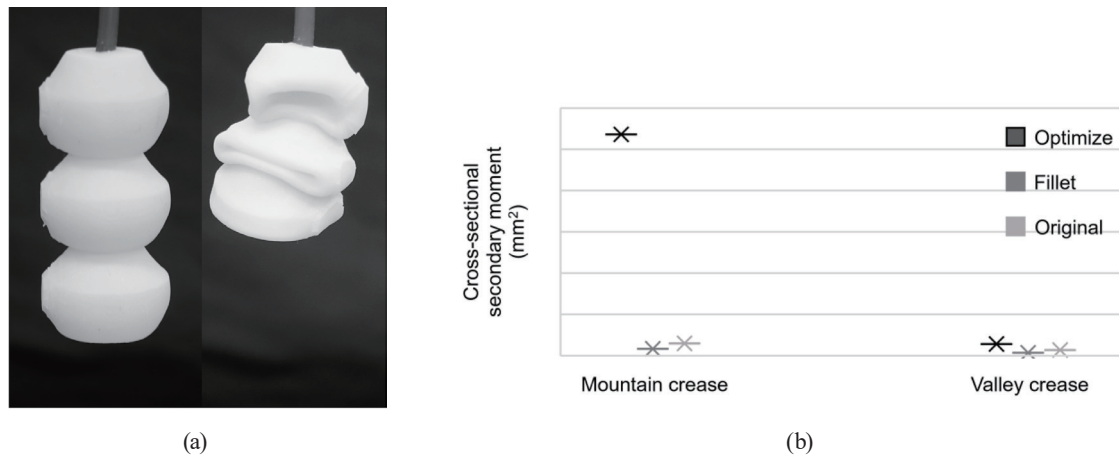


Fig. 11. (a) Deformation of linear model with filleted creases. (b) Second moment of area (about an axis parallel to line AB through the centroid of the cross-sectional crease shapes in Fig. 6) in the mountain and valley creases.

lying on the floor. The two model actuators lasted more than 100000 cycles (Table 1). The results show very high durability. Eliminating the bending stress concentration on the creases, which is the main breakdown cause of folding actuators, led to these results.

5. Discussion

Optimizing the creases to minimize the maximum bending stress may provide additional benefits aside from durability. We created another actuator that has filleted creases without the optimization. However, this actuator could not invaginate along the designed deformation, because the mountain crease was folded in the opposite way [Fig. 11(a)]. In other words, the module collapsed, ignoring the designed creases. We attribute the successful deformation of the crease-optimized actuator to an increased bending stiffness *along the crease curve* to avoid such collapse. This bending stiffness is expressed as the product of Young's modulus and the second moment of area. Figure 11(b) shows that the second moment of area of the optimized mountain crease is considerably larger than that of the before-optimized (original) and filleted creases.

When resizing the actuators, it is necessary to review the material, the thicknesses of the thick and thin membranes, and the size of the creases. When increasing the size of the actuator, the weight of the actuator is an issue, so appropriate wall thinning is necessary. Reducing the actuators' size requires 3D printers that can accurately form thin membranes.

6. Conclusion and Future Work

A vacuum-type soft pneumatic actuator was developed using invaginate deformation. In this study, the linear and bending deformation models were fabricated and evaluated. Using the invaginating design method, we achieved the desired transformation (large linear and bending

displacements) of the actuator. In addition, we incorporated creases that are highly durable to bending into the actuator, obtained by optimization to minimize the maximum bending stress on the cross-sectional crease shapes.

In future tasks, the deformation of the actuator needs to be controlled by applying various pressures to broaden its usage. We would also like to improve the performance of the actuators (by fabricating them using other materials), such as the manipulation of the blocked and lifting forces for handling materials. Design methods using symmetry surfaces and optimization for creases would be applicable to actuators driven by a positive air pressure source.

Acknowledgments

This work was supported by KAKENHI Grant-in-Aid for Scientific Research on Innovative Areas "Science of Soft Robot" project funded by JSPS under Grant Number 18H05467, and Grant-in-Aid for Scientific Research (B) under Grant Number 21H01289.

References

- 1 H. Adachi, K. Matsuda, T. Niimi, S. Kondo, and H. Gotoh: *Sci. Rep.* **10** (2020) 18687. <https://doi.org/10.1038/s41598-020-75709-y>
- 2 C. Tawk, G. M. Spinks, M. in het Panhuis, and G. Alici: *IEEE/ASME Trans. Mechatron.* **24** (2019) 2118. <https://doi.org/10.1109/TMECH.2019.2933027>
- 3 Y. Noma, K. Narumi, F. Okuya, and Y. Kawahara: *UIST '20: Proc. 33rd Annu. ACM Symp. User Interface Software and Technology* (2020) 58. <https://doi.org/10.1145/3379337.3415853>
- 4 M. A. Robertson and J. Paik: *Sci. Robot.* **2** (2017) eaan6357. <https://doi.org/10.1126/scirobotics.aan6357>
- 5 D. Yang, B. Mosadegh, A. Ainla, B. Lee, F. Khashai, Z. Suo, K. Bertoldi, and G. M. Whitesides: *Adv. Mater.* **27** (2015) 6323. <https://doi.org/10.1002/adma.201503188>
- 6 D. Yang, M. S. Verma, J.-H. So, B. Mosadegh, C. Keplinger, B. Lee, F. Khashai, E. Lossner, Z. Suo, and G. M. Whitesides: *Adv. Mater. Technol.* **1** (2016) 1600055. <https://doi.org/10.1002/admt.201600055>
- 7 D. Yang, M. S. Verma, E. Lossner, D. Stothers, and G. M. Whitesides: *Adv. Mater. Technol.* **2** (2017) 1600164. <https://doi.org/10.1002/admt.201600164>
- 8 B. Tondu: *J. Intell. Mater. Syst. Struct.* **23** (2012) 225. <https://doi.org/10.1177/1045389X11435435>
- 9 B. Tondu and P. Lopez: *IEEE Control Syst. Mag.* **20** (2000) 15. <https://doi.org/10.1109/37.833638>
- 10 K. Suzumori, S. Endo, T. Kanda, N. Kato, and H. Suzuki: *IEEE Int. Conf. Robot. Autom.* (2007) 4975. <https://doi.org/10.1109/ROBOT.2007.364246>
- 11 F. Ilievski, A. D. Mazzeo, R. F. Shepherd, X. Chen, and G. M. Whitesides: *Angew. Chem.* **123** (2011) 1930. <https://doi.org/10.1002/ange.201006464>
- 12 R. Niiyama, X. Sun, C. Sung, B. An, D. Rus, and S. Kim: *Soft Robot.* **2** (2015) 59. <https://doi.org/10.1089/soro.2014.0023>
- 13 D. Rus and M. T. Tolley: *Nat. Rev. Mater.* **3** (2018) 101. <https://doi.org/10.1038/s41578-018-0009-8>
- 14 M. A. Robertson, O. C. Kara, and J. Paik: *Int. J. Robot. Res.* **40** (2021) 72. <https://doi.org/10.1177/0278364920909905>
- 15 L. Paez, G. Agarwal, and J. Paik: *Soft Robot.* **3** (2016) 109. <https://doi.org/10.1089/soro.2016.0023>
- 16 S. Li, D. M. Vogt, D. Rus, and R. J. Wood: *Proc. Natl. Acad. Sci.* **114** (2017) 13132. <https://doi.org/10.1073/pnas.1713450114>
- 17 S. Suzuki: *Topology-driven form-finding: interactive computational modelling of bending-active and textile hybrid structures through active-topology based real-time physics simulations, and its emerging design potentials* (Institut für Tragkonstruktionen und Konstruktives Entwerfen, Universität Stuttgart, Stuttgart, 2020) (in German). <https://doi.org/10.18419/opus-10865>